© 2015. Published by The Company of Biologists Ltd | The Journal of Experimental Biology (2015) 218, 864-875 doi:10.1242/jeb.114280

RESEARCH ARTICLE

Body saccades of *Drosophila* consist of stereotyped banked turns

Florian T. Muijres[1,2,‡], Michael J. Elzinga[1], Nicole A. Iwasaki[1] and Michael H. Dickinson[1,*]

ABSTRACT

The flight pattern of many fly species consists of straight flight segments interspersed with rapid turns called body saccades, a strategy that is thought to minimize motion blur. We analyzed the body saccades of fruit flies (*Drosophila hydei*), using high-speed 3D videography to track body and wing kinematics and a dynamically scaled robot to study the production of aerodynamic forces and moments. Although the size, degree and speed of the saccades vary, the dynamics of the maneuver are remarkably stereotypic. In executing a body saccade, flies perform a quick roll and counter-roll, combined with a slower unidirectional rotation around their yaw axis. Flies regulate the size of the turn by adjusting the magnitude of torque that they produce about these control axes, while maintaining the orientation of the rotational axes in the body frame constant. In this way, body saccades are different from escape responses in the same species, in which the roll and pitch component of banking is varied to adjust turn angle. Our analysis of the wing kinematics and aerodynamics showed that flies control aerodynamic torques during the saccade primarily by adjusting the timing and amount of span-wise wing rotation.

KEY WORDS: Insect, Biomechanics, Flapping wing, Aerodynamics, Maneuvering flight, Flight control, Wingbeat kinematics

INTRODUCTION

When exploring a local environment, many species of fly exhibit a flight pattern consisting of straight segments interspersed with rapid turns called body saccades (Collett and Land, 1975; Tammero and Dickinson, 2002; Wagner, 1986; Wehrhahn et al., 1982). This distinct flight pattern might serve many functions, but one likely advantage is that the quick turns allow flies to restrict the time periods during which their visual system is severely compromised by motion blur (Collett and Land, 1975; Hateren and Schilstra, 1999; Land, 1999; Schilstra and Hateren, 1999). Whatever the function, it appears to be the preferred means of changing direction in some species. For example, a recent analysis of *Drosophila melanogaster* found that more than 80% of all changes in heading occur via body saccades (van Breugel and Dickinson, 2012).

There is some controversy regarding the neural mechanisms that trigger saccades in *Drosophila* (Dickinson, 2014). Several studies of both free and tethered flight behavior suggest that most saccades are triggered by visual expansion and thus represent collision-avoidance reflexes that protect flies from flying into large obstacles or avoiding clutter (Censi et al., 2013; Reiser and Dickinson, 2013; Stewart et al., 2010; Tammero and Dickinson, 2002). Other studies, however, suggest that some saccades are triggered internally by a deliberately stochastic process that functions to optimize the animal's search efficiency (Maye et al., 2007; Reynolds and Frye, 2007). In addition, flies exhibit rapid turns in other contexts, such as when they lose contact with an odor plume (van Breugel and Dickinson, 2014), or in response to a rapid visual expansion as might be created by an approaching predator (Muijres et al., 2014). It is not known, however, whether rapid turns elicited by different stimuli or internal triggers operate via a single common motor program.

The aerodynamic basis of saccades, which is the main subject of this paper, has been investigated previously by Fry and co-workers using the fruit fly *Drosophila melanogaster* (Fry et al., 2003). Based on a relatively small number of high-speed video sequences, these authors proposed a model in which flies change course primarily by creating torque around their yaw axis (defined in that study as perpendicular to the longitudinal body axis), which they accomplish by simultaneously changing stroke amplitude and deviations out of the stroke plane. In addition, these authors reported that the changes in wing kinematics were biphasic, which they interpreted as indicating that flies generate first torque and then counter-torque during each maneuver. Finally, they presented a simple model in which the dynamics about the yaw axis were dominated by inertia during the brief maneuvers, consistent with the production of counter-torque (Fry et al., 2003). Subsequent authors, however, challenged some conclusions of this simple model. Hesselberg and Lehmann (2007) noted that because of the reciprocating pattern of wing motion, the damping about the yaw axis is quite large and should quickly dominate dynamics during turns – a calculation that was supported by subsequent models and measurements (Cheng et al., 2010; Dickson et al., 2010). Hedrick and co-workers (2009) went so far as to suggest that animals over a very large size range need only produce a small amount of counter-torque during saccades, and can rely primarily on passive damping to coast to a stop after initiating a turn. Further, studies of corrective maneuvers in *Drosophila* suggested that flies generate yaw torque by regulating the angle of attack of the wing during the upstroke and downstroke, and not by altering either stroke amplitude or stroke deviation (Bergou et al., 2010).

In this paper, we employed 3D high-speed videography to capture the wing and body motion of the fruit fly *Drosophila hydei* Sturtevant 1921 during free-flight body saccades. Although this study repeats the basic paradigm developed by Fry and co-workers over a decade ago (Fry et al., 2003), the improvements in high-speed cameras as well as the utility of an automated machine vision-tracking system allowed us to revisit saccade dynamics with greater resolution and statistical rigor. The results demonstrate that body saccades are a remarkably stereotyped behavior combining a brief banked turn (requiring rotation and counter-rotation in roll and pitch) with a unidirectional rotation about the yaw axis. By measuring the changes in wing motion during saccades and using a dynamically scaled robot, we were able to determine the relative importance of different features of wing motion in generating forces

[1]Department of Biology, University of Washington, Seattle, WA 98195, USA.
[2]Experimental Zoology Group, Wageningen University, De Elst 1, 6708 WD, Wageningen, The Netherlands.
*Present address: California Institute of Technology, Pasadena, CA, USA.

‡Author for correspondence (florian.muijres@wur.nl)

Received 22 September 2014; Accepted 12 January 2015

List of symbols and abbreviations

A	amplitude
$\mathbf{a}=\{a_x, a_y, a_z\}$	acceleration vector in the world reference frame
a_{hor}	horizontal acceleration
a_n	Fourier series coefficient
a_N	horizontal acceleration normal to the flight path
a_T	horizontal acceleration tangential to the flight path
a_z	vertical acceleration
b_n	Fourier series coefficient
C	normalized aerodynamic damping coefficient matrix
dt	time step between measurements (inverse of camera frame rate)
dU	flight speed relative to the start of the maneuver
f	wingbeat frequency
F	normalized aerodynamic force vector in the world reference frame
g	gravitational acceleration scalar
$\mathbf{g}=\{0,0,g\}$	gravitational acceleration vector
I	normalized inertia coefficient matrix
l	wing length
m	body mass
mg	body weight
Q	process noise covariance matrix of Kalman filter
R	measurement noise covariance matrix of Kalman filter
t	time relative to the start of the saccade
T	normalized aerodynamic torque vector in the body reference frame
T′	an arbitrarily defined aerodynamic torque vector
t^*	normalized time within a wingbeat relative to the start of the downstroke
$\mathbf{U}=\{u,v,w\}$	velocity vector in the world reference frame
$\mathbf{X}=\{x,y,z\}$	position vector in the world reference frame
$\mathbf{X_B}=\{x_B,y_B,z_B\}$	position vector in the body reference frame
α	rotation angle of the wing around its long axis
β	pitch angle of the aerodynamic force vector in the body reference frame
γ	deviation angle of the wing out of the stroke plane
Δt	duration of a saccadic turn
$\Delta\alpha$	shift of the mean wing rotation angle of the left wing relative to the right
$\Delta\kappa$	shift of the mean wing kinematics angle of the left wing relative to the right
$\Delta\sigma$	turn angle of the saccade
$\Delta\tau$	phase shift of the left wing movement relative to the right wing movement
η	body roll angle derived from roll rate ω_x
η_E	body roll Euler angle in the world reference frame
θ	body pitch angle derived from pitch rate ω_y
θ_E	body pitch Euler angle in the world reference frame
κ	wing kinematics angle
μ	torque axis angle within the stroke plane relative to the roll torque axis
μ_1	primary torque axis angle (mean torque angle during the initial phase of the banked turn)
μ_2	counter-torque axis angle (mean torque angle during the counter-torque phase of the banked turn)
$\mu_{1\perp}$	angle within the stroke plane and orthogonal to μ_1
$\mu_{2\perp}$	angle within the stroke plane and orthogonal to μ_2
ξ	roll angle of the aerodynamic force vector in the body reference frame
σ	heading (the direction of the horizontal body velocity component)
σ_a	direction of the horizontal body acceleration component
τ	phase within a wingbeat relative to the start of the downstroke
ϕ	stroke angle of the wing within the stroke plane
ψ	body yaw angle derived from yaw rate ω_z
ψ_E	body yaw Euler angle in the world reference frame
$\mathbf{\Omega}=\{\omega_x, \omega_y, \omega_z\}$	normalized rotation rate vector of the body in the body reference frame
ω_x	normalized body roll rate in the body reference frame
ω_y	normalized body pitch rate in the body reference frame
ω_z	normalized body yaw rate in the body reference frame

and torques. The results help to resolve some of the recent controversies regarding the dynamics of saccadic turns in *Drosophila* and other insects.

RESULTS

We tracked a total of 44 flight sequences (Fig. 1, see Materials and methods), each consisting of a straight flight segment followed by a single body saccade (see supplementary material Movies 1 and 2). Assuming that there is no difference between left- and right-hand turns, we mirrored all left-hand turns, and then aligned all sequences based on time and heading with respect to the start of the saccade (Fig. 1E,F; see also supplementary material Movies 3–6). Heading is defined as the angular direction of the flight path, not the body orientation. The saccadic turn angles ($\Delta\sigma$), which quantify the total angular change in heading, varied substantially among saccades from approximately 20 deg to almost 180 deg (Fig. 1E,F and Fig. 2A,B), with an average of 93 ±27 deg (mean±s.d., N=44). During the maneuvers, flight speed tended to dip briefly and then gradually rise (Fig. 2C). The duration of turn ($\Delta t=t_{stop}-t_{start}$) was 49±18 ms ($N$=44), or approximately nine wingbeats, although this is an underestimate of the entire maneuver because t_{start} and t_{stop} were defined using finite thresholds (see Materials and methods). These basic saccade metrics are similar to those previously reported on free-flying *D. melanogaster* (Tammero and Dickinson, 2002; Fry et al., 2003; van Breugel and Dickinson, 2012).

To examine how flies alter heading during saccades, we measured the magnitude and direction of horizontal and vertical accelerations throughout the maneuver (Fig. 2D–F). Immediately at the start of the saccade, flies generate a horizontal force that results in a sideways acceleration. The magnitude (a_{hor}/g) of this sideways acceleration first increases and then decreases (Fig. 2E), while its orientation (σ_a) remains relatively constant (Fig. 2D). Vertical acceleration (a_z/g) remains near zero throughout the entire maneuver (Fig. 2F).

The time course of roll rate, pitch rate and yaw rate during the maneuvers (Fig. 1C and Fig. 2G–I) along with their integrals and derivatives (supplementary material Fig. S1) show that flies rotate about all principal body axes, and thus body saccades constitute a banked turn. Flies also increase force production so the vertical component remains roughly equal to body weight (Fig. 2F,J). The orientation of **F** in the body reference frame remains constant (Fig. 2K,L), consistent with the so-called 'helicopter model' of insect flight (David, 1978; Götz and Wandel, 1984). Thus, as with more rapid escape maneuvers (Muijres et al., 2014), a fly generates sideways accelerations during saccades by rotating its body rather than by adjusting the orientation of the force vector in the body frame.

To determine how the flies control roll, pitch and yaw throughout the saccade, we estimated torque about these axes as the sum of torque required to overcome inertia (inertia torque) and torque required to overcome damping (damping torque) (Fig. 3, see Eqn 2

The Journal of Experimental Biology (2015) 218, 864-875 doi:10.1242/jeb.114280

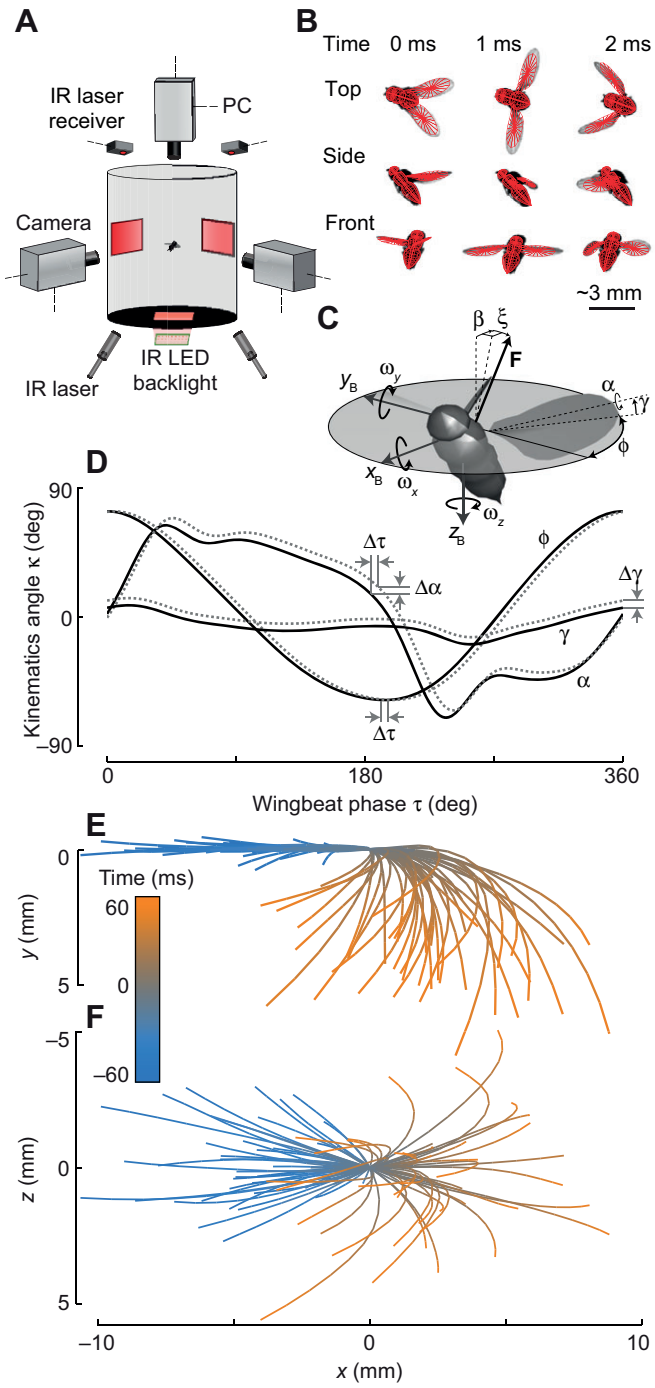

Fig. 1. Experimental setup, coordinate system conventions, and flight tracks of saccades. (A) The experimental setup consists of a cylindrical enclosure, three synchronized high-speed cameras with infrared LED backlighting, and a laser triggering system. (B) An automated machine vision system tracks kinematics by projecting body and wing models onto the three orthogonal camera images. (C) Measured parameters in the body reference frame. Body dynamics are described by the angular velocity vector of the body, $\mathbf{\Omega}=\{\omega_x,\omega_y,\omega_z\}$, and its derivatives, about the principal body axes $\mathbf{X_B}=\{x_B,y_B,z_B\}$. Wing kinematics are defined by stroke angle within the stroke plane ϕ, deviation angle out of the stroke plane γ, and wing rotation angle α. Based on the vector sum of body acceleration and the gravitational acceleration vector, we determined the normalized force vector **F**, with orientation in the body reference frame defined as force pitch angle β and roll angle ξ. (D) Temporal dynamics of the wing kinematics angles for a single wingbeat. The black trace shows the average steady wingbeat of *D. hydei* that is used as a baseline for our analysis (from Muijres et al., 2014). Gray traces show hypothetical wing angles: stroke angle has a phase shift of $\Delta\tau$=5 deg relative to the steady wingbeat, wing deviation has a mean deviation angle shift of $\Delta\gamma$=5 deg, and wing rotation angle has a shift of both $\Delta\tau$=5 deg and $\Delta\alpha$=5 deg. (E,F) Top view (E) and side view (F) of the flight tracks of all 44 trials. Traces are color coded with time according to the scale bar in E. Note that all left-hand turns have been mirrored into right-hand turns, and all sequences were aligned according to position and heading at the start of the saccadic maneuver (t_{start}=0 ms).

in Materials and methods). Torque about the yaw axis consists mostly of damping torque, confirming that yaw rotations during a saccade are highly damped (Hedrick et al., 2009; Hesselberg and Lehmann, 2007). In contrast, torque about the roll axis consists about equally of inertial torque and damping torque, whereas damping torque about the pitch axis is negligible compared with inertial torque. The fact that rotations about the pitch axis are poorly damped during saccades is supported by a recent study of forward flight dynamics in fruit flies (Elzinga et al., 2014).

A simple means of implementing a banked turn would be to rotate the body about a fixed axis in the stroke plane and then to counter-rotate to continue level flight, while at the same time generating a yaw rotation to align body orientation with the new flight heading. The magnitude of the turn could then be adjusted by regulating the amount of torque produced, and not its direction. Evidence that flies might implement such a simple control scheme is shown in Fig. 4. The torque vectors for the primary rotation phase and the counter-rotation phase for all 44 sequences (in blue and orange, respectively) aligned remarkably well (Fig. 4A,B). The average torque vector axes for the initial rotation and counter-rotation are defined as the primary torque axis μ_1 and the counter-torque axis μ_2, which are oriented 36 and 8 deg from the longitudinal body axis, respectively. The time history of the direction (Fig. 4A) and magnitude (Fig. 4C,D) of the torque component in the stroke plane exhibits a biphasic shape indicative of rotation and counter-rotation about the μ_1 and μ_2 axis, respectively (Fig. 4C). In contrast, little torque is generated about the orthogonal axes ($\mu_{1\perp}$ and $\mu_{2\perp}$, respectively, Fig. 4D; see also supplementary material Fig. S2). Thus, animals execute the banked turn by generating torque and counter-torque about two control axes (μ_1 and μ_2) whose orientation remains constant from saccade to saccade (Fig. 4A,B). The magnitude of the torque produced about the control axes, however, does correlate with the turn angle $\Delta\sigma$ (Fig. 4F), which suggests the mechanism by which flies regulate the size of the heading change.

Simultaneously with the rotations about the μ_1 and μ_2 axes, but within a longer time scale, flies generate a unidirectional yaw torque in the same direction as the change in heading (Fig. 4E). Also, the magnitude of mean yaw torque during the turn is positively correlated with turn angle (Fig. 4H). Although not necessary for changing the direction of the flight path, the yaw rotation is required to align the longitudinal body axis with the new heading. This correction to minimize sideslip is not fully completed in most sequences because of limitations of our visualization volume (Fig. 4E). Note that by rotating about the yaw axis while its body is banked, the fly will generate a head-down movement within the world frame of reference. This could explain why the initial body rotation axis μ_1 and counter-rotation axis μ_2 are not aligned and μ_2 includes a smaller pitch (down) component.

The sequence of 21 averaged wingbeats (N=44 trials) show that all kinematics parameters (wingbeat frequency, stroke angle, deviation angle and wing rotation angle, Fig. 1C) change during a saccade, and that these modifications are all very subtle (Fig. 5A–G). Wingbeat frequency increases by only a few hertz and all modifications in wing

The Journal of Experimental Biology (2015) 218, 864-875 doi:10.1242/jeb.114280

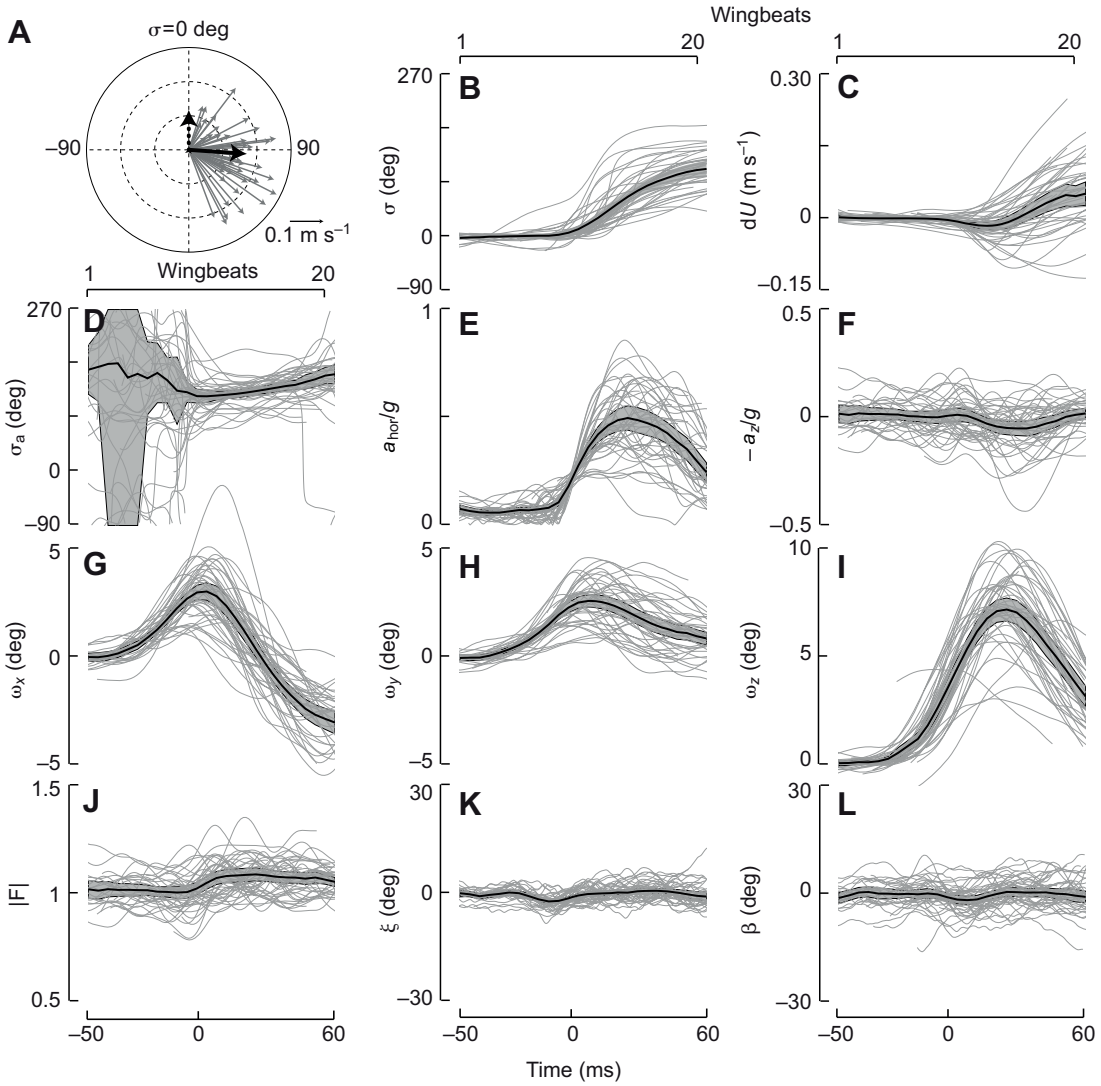

Fig. 2. Saccades in flies consist of banked turns. (A) Heading σ and speed (depicted as vectors of the horizontal velocity component) after the saccades for all measured trials separately (gray) and its mean (black solid vector), relative to the aligned initial zero heading (black dotted mean velocity vector). Speed is scaled according to the reference vector of 0.1 m s^{-1}. (B–L) temporal dynamics of experimental parameters. (B) Heading relative to initial heading of 0 deg (σ). (C) Changes in flight speed relative to initial flight speed (d*U*). (D) Direction of the horizontal component of body acceleration in the world reference frame (σ_a). (E) Horizontal component of normalized body acceleration (a_{hor}/g). (F) Vertical component of normalized body acceleration, a_z/g (negative values are shown such that upwards accelerations are in the positive *y*-axis direction). (G–I) Normalized roll rate (ω_x; G), pitch rate (ω_y; H) and yaw rate (ω_z; I). (J) Normalized aerodynamic force generated by the fruit fly (|**F**|). (K,L) Roll angle (ξ; K) and pitch angle (β; L) of **F** (see also Fig. 1C). In B–L, gray traces depict data from separate trials and black traces with gray bars show the mean and 95% confidence interval for all trials.

angles are less than 5 deg. Nevertheless, replaying the averaged kinematics sequence on the robotic fly generated normalized forces (|***F***|) and torques (T_{roll}, T_{pitch} and T_{yaw}) that were similar to those estimated from body dynamics (using Eqns 1 and 2 in Materials and methods, respectively; Fig. 5H–K). For example, the time history for the torque about the roll axis measured on the robotic fly exhibits the torque and counter-torque that is predicted from body dynamics (Fig. 5I). Thus, although the measured changes in wing motion are subtle, they appear sufficient to capture the requisite changes in forces and moments reasonably well. Because the robotic fly is fixed and cannot translate and rotate in response to the forces and moments it generates, we did not expect (nor obtain) a perfect match between the measured forces and moments and those calculated from body dynamics.

To better understand how flies modulate wingbeat kinematics to control torque around each individual control axis during a saccade, we extracted the wing kinematics associated with peak torque about the μ_1, μ_2 and yaw axes from the entire dataset and replayed these kinematics on the robotic fly (Fig. 6, see Materials and methods). The kinematics correlated with peak torque production exhibit distortion of all three wing angles (Fig. 6A–C) and, when played through the robot, produced the expected torques (Fig. 6D–F). The fly's wing motion is able to create positive yaw torque throughout almost the entire wingbeat, with the exception of brief periods during stroke transitions (Fig. 6D). In contrast, torque production about the μ_1 and μ_2 axes is more complicated in that the time history includes both positive and negative excursions and the magnitude of the transient peaks is quite large relative to the average value (Fig. 6E). Most of the variations in torque production relative to the torque generated by the steady flight wingbeat (i.e. the symmetric wingbeat that produced weight support and no net torque, Fig. 1D), occur at the start of the upstroke and downstroke, just after stroke

The Journal of Experimental Biology (2015) 218, 864-875 doi:10.1242/jeb.114280

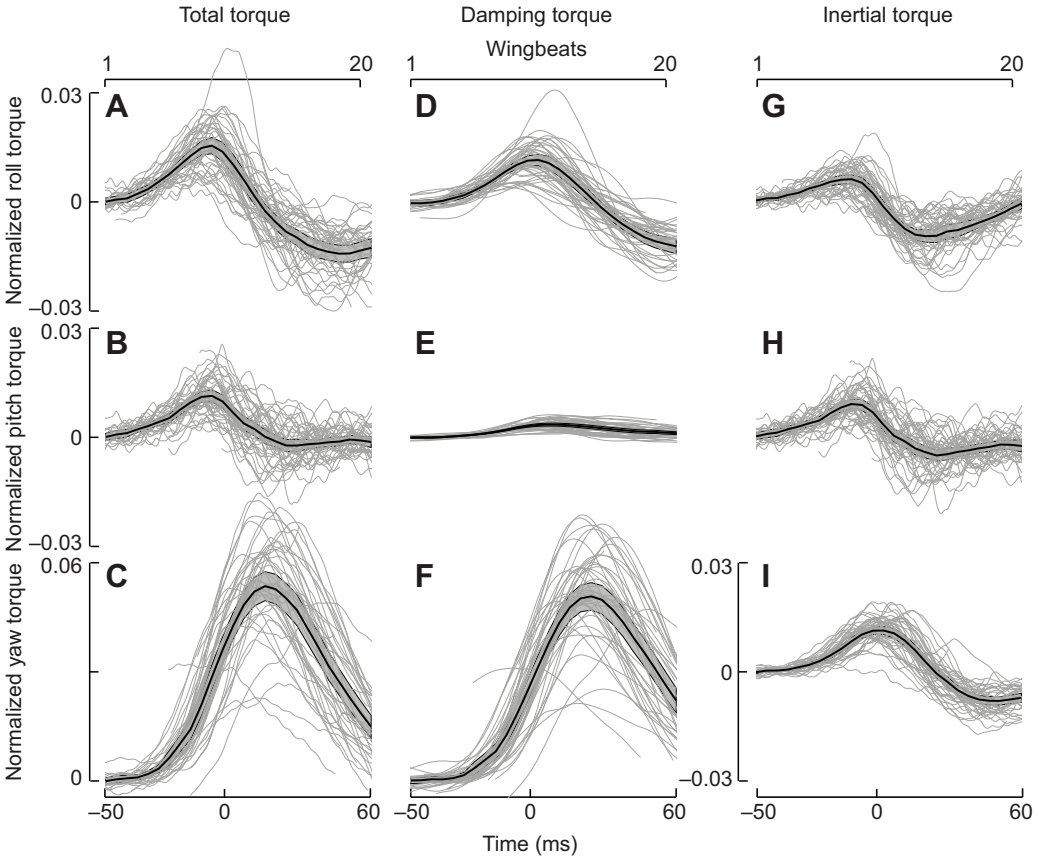

Fig. 3. Throughout a saccade, flies produce torque about all body axes: the roll axis, pitch axis and yaw axis. The total normalized body torque (A–C) is the sum of torques required to resist aerodynamic damping (D–F) and to resist inertia (G–I). All torques are defined in the body reference frame (Fig. 1C) and normalized by $|\boldsymbol{a}+\boldsymbol{g}|ml$ (see Eqn 2 in the Materials and methods). Gray lines show data from the separate saccade; black lines with gray bars are means and 95% confidence intervals for all trials.

reversal (Fig. 6E). The wingbeat patterns that generate peak torque about the μ_1 and μ_2 axes create very little mean torque about the orthogonal axes ($\mu_{1\perp}$ and $\mu_{2\perp}$), even though the magnitude of the oscillations through the stroke is quite large (Fig. 6F).

Next, we constructed a set of systematically distorted stroke patterns ranging from steady flight conditions to kinematics that generate peak torque about the μ_1, μ_2 and yaw axes, and then replayed these on the robot (see Materials and methods). For yaw, torque measured using the robot matched the values derived from body motion (Eqn 1) throughout the entire range of distorted kinematics (average difference ~2%, Fig. 7A). For the μ_1 and μ_2 axes, the torques derived from body motion are about 66% and 59% (respectively) that measured with the robotic fly, suggesting that the dynamic model for roll and pitch (Eqns 2–4) may be oversimplified or that the torque measured using a robot in a fixed reference frame does not accurately model the free-flight case. We also measured the cross-talk (i.e. the torque generated around orthogonal axes) produced by the kinematics associated with production of peak torque around the different torque axes. For the yaw case, the cross-talk about the roll and pitch axes was −24% and 27% of $|\mathbf{T}_{\mathrm{yaw}}|$, respectively (Fig. 7A). For the μ_1 case, the cross-talk about the $\mu_{1\perp}$ and yaw axes was 3% and 45% of $|\mathbf{T}_{\mu_1}|$, respectively, and for the μ_2 case, the cross-talk around the $\mu_{2\perp}$ and yaw axes was 23% and 47% of $|\mathbf{T}_{\mu_2}|$, respectively (Fig. 7B). The cross-talk between the yaw torque and torque about the axes in the stroke plane (Fig. 7A,B) shows that our method did not enable us to completely separate the effect of torque and force production about the different principal axes. This is most likely due to the fact that during saccadic maneuvers, flies increase force production and produce torque about the different axes in synchrony. So, wingbeats that produced large torque about the axes in the stroke plane tended to also produce high yaw torque and increased aerodynamic forces (Fig. 5).

Next, we varied the kinematics for each of the three wing angles in isolation to determine their relative contribution to torque (Fig. 7C,D). As was also the case for evasive maneuvers (Muijres et al., 2014), the sum of torques resulting from modulating the different components of wing motion separately matches the torque generated by modulating all components simultaneously, indicating a remarkable degree of linearity. For all torque axes, wing rotation angle had the strongest effect on changes in total torque, whereas changes in stroke amplitude and stroke deviation contribute modestly to the control of torque around the μ_1 and μ_2 axes and make almost no contribution to the control of yaw torque (Fig. 7C,D).

As suggested by a previous study of *D. melanogaster*, a change in the mean offset of the rotation angle will create yaw torque by increasing the angle of attack during one half-stroke and decreasing it on the other (Bergou et al., 2010). However, another means by which wing rotation might influence torque is through changes in the timing of wing rotation relative to stroke reversal, which can change forces via unsteady mechanisms (Dickinson et al., 1999). To explore the relative importance of these two potential mechanisms, we estimated both the relative phase shift and mean offset of the time course of the wing kinematics angles for the left and right wings during the strokes that generated peak torque (Fig. 8;

The Journal of Experimental Biology (2015) 218, 864-875 doi:10.1242/jeb.114280

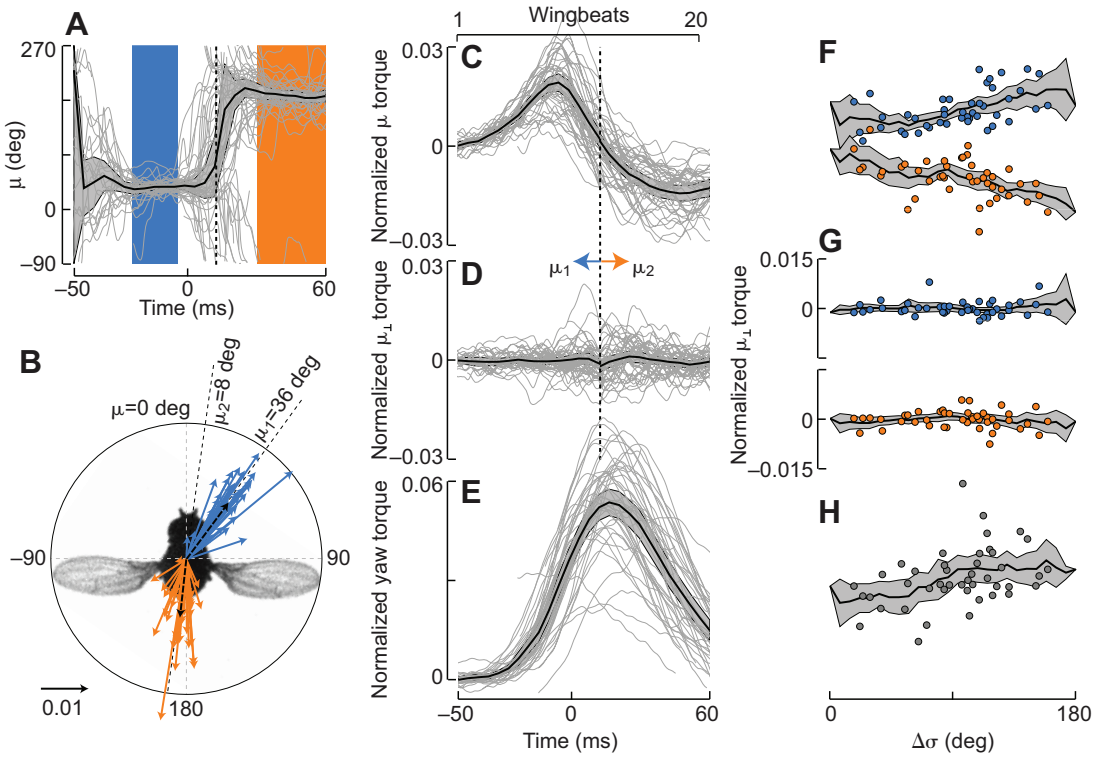

Fig. 4. The early stage of a saccade can be separated into two phases, an initial body rotation (–25 ms<*t*<–5 ms) and a counter-rotation (30 ms<*t*<60 ms). During each phase (initial body rotation data in blue; counter-rotation data in orange), flies produce torque about two body axes and keep torque about the third orthogonal axis to a minimum. (A) Direction of torque within the stroke plane, μ, throughout the saccade. (B) Vectors depicting the orientation and magnitude of the torque component within the stroke plane, $\mathbf{T}_{\mu}$, during the initial rotation phase and the counter-rotation phase (see A for the time windows). The black dashed vectors are mean $\mathbf{T}_{\mu}$ for both time windows, defining the primary torque axis (μ_1=36 deg) and the counter-torque axis (μ_2=8 deg). Normalized torque vectors are scaled according to the reference vector of 0.01. (C) Torque about the primary torque axis μ_1 (*t*<12.5 ms) and the counter-torque axis μ_2 (*t*>12.5 ms). (D) Torque about the orthogonal axes $\mu_{1\perp}$ (*t*<12.5 ms) and $\mu_{2\perp}$ (*t*>12.5 ms). (E) Torque about the yaw axis. (F) Average magnitude of normalized body torque relative to turn angle Δσ about the μ_1 (blue) and μ_2 (orange) axes. (G) Torques about their orthogonal $\mu_{1\perp}$ and $\mu_{2\perp}$ axes. (H) Torque about the yaw axis. All torques are defined in a right-handed reference frame relative to the μ_1, μ_2 and yaw axes and were normalized by |**a**+**g**|*ml*. In A, C, D and E, gray lines show data from all measured saccades; black lines with gray bars are means and 95% confidence intervals.

supplementary material Fig. S3). Fig. 8C–F shows that there is a phase shift of ~5 deg in the wing rotation angle of the left wing relative to the right wing during wing strokes that produce peak torque around the μ_1 and μ_2 axes, but there is no evidence for a change in mean offset. In the case of yaw torque, a phase shift of ~3 deg is accompanied by an offset of ~4 deg. Thus, although torque about the yaw, μ_1 and μ_2 axes is primarily controlled by changes in the time course of wing rotation, our results suggest that the relative mechanisms are different. Flies regulate the torque about the μ_1 and μ_2 axes by modulating unsteady rotational lift mechanisms during stroke reversal (Dickinson et al., 1999), whereas yaw torque is controlled by a combination of unsteady effects at stroke reversal and differences in drag during the translational phase of the two half-strokes (Bergou et al., 2010). This interpretation is consistent with the time history of the changes in torque throughout the wingbeat for the kinematics that produce peak torques (Fig. 6). Yaw torque is produced mostly during the translation phase of the wingbeat (Fig. 6D), which is indicative of an asymmetry in drag production between the two wings. In contrast, changes in torque about the μ_1 and μ_2 axes (relative to a steady wing stroke) occur mostly at the start of each wingstroke (Fig. 6E), suggesting modulations in rotational effects.

DISCUSSION

Our analysis showed that fruit flies perform body saccades by executing stereotyped banked turns (Fig. 2). The axes of the initial rotation (μ_1) and subsequent counter-rotation (μ_2) are aligned 36 and 8 deg from the roll axis of the fly, respectively (Fig. 4B). Flies control the size of the turn by regulating the magnitude of torque around these rotation axes (Fig. 4F), and not by adjusting their orientation as they do during more rapid escape maneuvers (Muijres et al., 2014). Flies also rotate unidirectionally around the yaw axis during saccades to correct for the misalignment between body orientation and heading (i.e. sideslip) that accumulates as a result of the banked turn.

Using a simple dynamic model, we were able to estimate the relative contribution of inertia and damping during a saccade (Fig. 3). We found that yaw dynamics are dominated by passive damping that results from the reciprocal flapping pattern, as suggested by Hesselberg and Lehmann (2007). Pitch dynamics, in contrast, are dominated by inertia, and the contribution of damping and inertia in roll dynamics is roughly equal. Thus, saccade dynamics are quite complex and accurate models must include both inertial and damping terms (Bergou et al., 2010; Cheng et al., 2010; Dickson et al., 2010; Fry et al., 2003; Hedrick et al., 2009; Hesselberg and Lehmann, 2007). The model for rapid turns proposed by Hedrick and co-workers (2009) in which insects rely primarily on passive damping to generate counter-torque may not be as general as proposed, assuming that other insects also employ banked turns and do not simply rotate about the yaw axis.

The maneuver that we have measured in fruit flies using high-speed videography is similar to the body saccades of blowflies,

The Journal of Experimental Biology (2015) 218, 864-875 doi:10.1242/jeb.114280

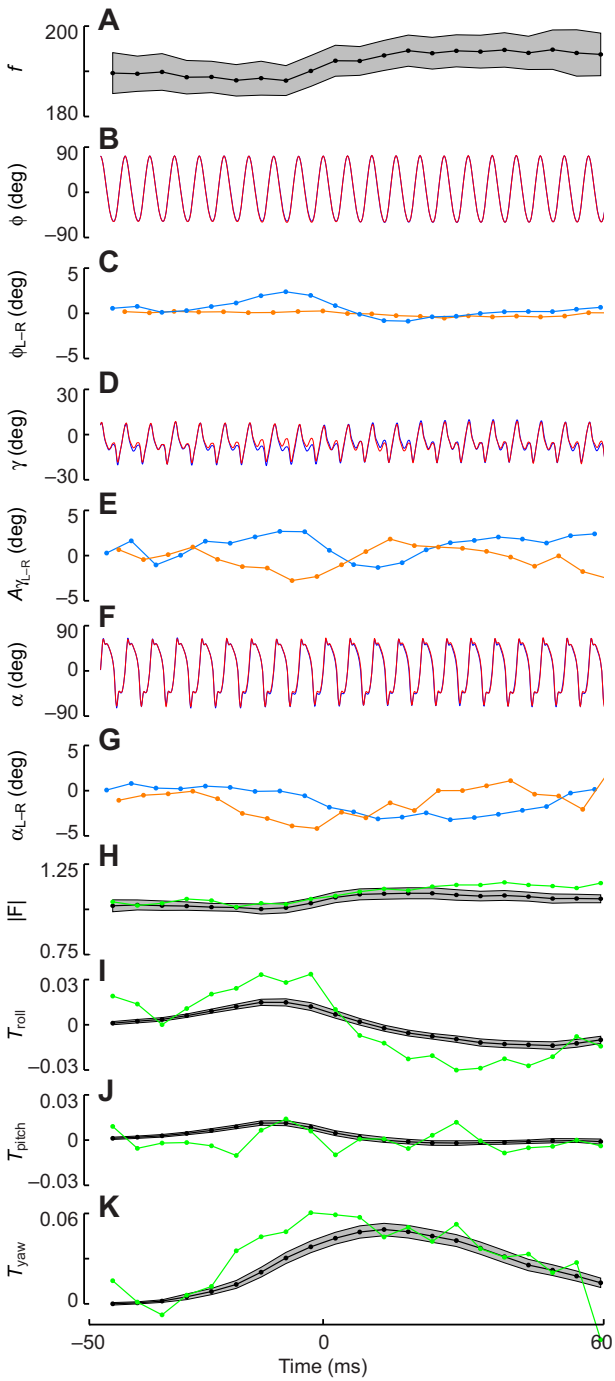

Fig. 5. The average wing and body kinematics, determined by aligning the wingbeats of all trials relative to the start of each saccade, show that flies produce aerodynamic torques throughout a saccade using small changes in their wing movement patterns. (A) Wingbeat frequency *f* (mean and 95% confidence interval). (B) Stroke angle ϕ for the left (blue) and right (red) wing. Note that the blue and red traces are so similar that they appear to be a single line. (C) Difference in stroke angle at the end of the downstroke (blue) and upstroke (orange). (D) Deviation angle γ. (E) Difference in deviation angle amplitude during the downstroke (blue) and upstroke (orange). (F) Wing rotation angle α. (G) Difference in wing rotation angle at mid-downstroke (blue) and mid-upstroke (orange). (H) Normalized stroke-averaged force |**F**| based on body accelerations (black trace for mean and gray bar for 95% confidence interval) and based on wing kinematics shown in B, D and F and robotic fly experiments (green trace). (I–K) Normalized roll torque T_{roll} (I), pitch torque T_{pitch} (J) and yaw torque T_{yaw} (K). Plotting conventions in I–K are the same as in H.

measured elegantly by Schilstra and Hateren (1999) using tiny inductive coils. Thus, at least two species of fly, encompassing a rather large range in scale, execute banked turns to produce rapid changes in flight direction. Given the high degree of similarity within their nervous systems, it is likely that the body saccades of *Drosophila* and *Calliphora* are generated by homologous circuits.

Visually elicited escape maneuvers (Muijres et al., 2014) and voluntary body saccades in fruit flies both consist of a banked turn, but the dynamics of the two maneuvers are different enough to suggest that they are produced by distinct motor programs. Although body saccades are fast, the changes in heading during an evasive maneuver are faster, consistent with a more pronounced rotation of the body that reorients the mean force vector to produce a larger horizontal component. As a consequence, flies do not maintain weight support during the initial stages of an escape maneuver, whereas they do during body saccades (Fig. 2F,J). Similarly, yaw is poorly controlled during the initial stages of an evasive maneuver, resulting in large sideslip angles that are corrected long after the fly changes heading. During a body saccade, the yaw correction is better coordinated with the banked turn, so that sideslip is minimized throughout the maneuver. Perhaps the greatest difference between the two maneuvers relates to the manner by which the magnitude of the change in heading is controlled. Flies regulate the turn angle of a saccade by varying torque magnitude about two highly stereotypic axes (μ_1 and μ_2), whereas during evasive maneuvers the turn angle is controlled by adjusting the direction of the body rotation axis within the stroke plane. One interpretation that unifies all these differences is that evasive maneuvers may be optimized to alter flight heading as quickly as possible at the expense of flight control and motion blur, whereas body saccades are optimized to restrict retinal slip to a brief period.

The transition from rotation to counter-rotation during a body saccade is quite fast and such a pattern might be generated in a feed-forward manner by a central motor program or, alternatively, the initial rotation might trigger the counter-rotation via a sensory-mediated reflex. The halteres are a likely source of such feedback, as they mediate compensatory reactions to imposed rotations (Dickinson, 1999; Nalbach, 1994; Ristroph et al., 2010; Sherman and Dickinson, 2003). Previous studies of saccades using a magnetic tether in which the animal is free to rotate about its yaw axis suggest that haltere feedback, but not visual feedback, plays a role in terminating saccades (Bender and Dickinson, 2006). Interpretation of these prior experiments using magnetic tethers is complicated, however, by the new free-flight data, which show that *Drosophila* bank to change direction at the start of the saccade. Given their time course, the slow unidirectional saccade-like rotations that flies exhibit on magnetic tethers most likely represent the slower yaw phase of a free-flight saccade. Thus, the manipulation experiments performed by Bender and Dickinson (2006) might indicate that haltere feedback is involved in regulating the duration of the slower yaw correction phase of a saccade but do not directly address the question of whether feedback triggers the faster counter-rotation phase of the initial banked turn.

By exploiting the high-throughput capabilities of our tracking system, we were able to make accurate measurements of the changes in wing motion during saccades (Fig. 6). All three wing angles (ϕ, γ, α) exhibit a biphasic modulation during the time course of the saccade, as expected from the production of torque and counter-torque (Fig. 5B–G). These data are consistent with the previous observations of Fry and co-workers (2003), although these authors misinterpreted this biphasic pattern as indicating active

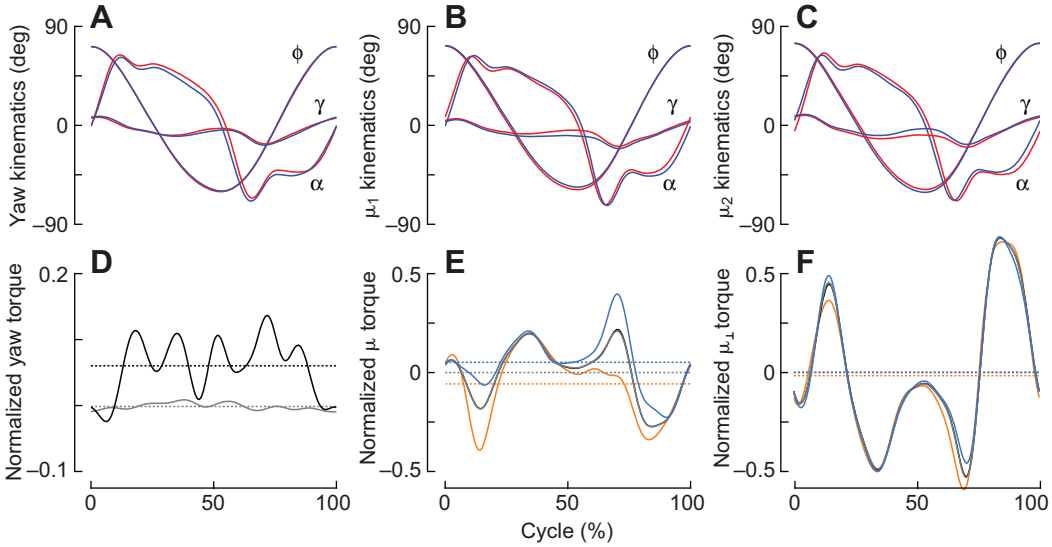

Fig. 6. Average wing kinematics angles and torque for wingbeats that generate peak torque about the control axes. (A–C) Kinematics angles for the left wing (blue) and for the right wing (red) for strokes that generated peak yaw torque (A), peak μ_1 torque (B) and peak μ_2 torque (C). (D) Normalized yaw torque measured by replaying wingbeat kinematics in A (black) and the steady flight kinematics in Fig. 1D (gray) on the robotic fly model. Solid lines are time series throughout the wingbeat, dotted lines are stroke-averaged values. (E) Normalized torque about the μ_1 axis for the kinematics in B (blue), normalized torque about the μ_2 axis for the kinematics in C (orange), and torque about the μ_1 and μ_2 axes for the steady flight wingbeat kinematics in Fig. 1D (black and gray, respectively). Note that the black and gray traces are so similar that they appear to be a single line. (F) Normalized torques about the $\mu_{1\perp}$ and $\mu_{2\perp}$ axes, using the color conventions as in E.

breaking around the yaw axis, when it is more likely that they observed evidence for the counter-rotation about the μ_2 axis. Replaying the pattern of wing motion on a stationary robot generated a time history of forces and moments that matched those derived from free-flight body dynamics reasonably well, but not perfectly (Fig. 5H–K). The match for total flight force and yaw was quite good, whereas roll torque based on the wing kinematics and the robot measurements was larger than roll torque derived from body dynamics. This mismatch is perhaps not too surprising, given that the saccade basically consists of a rapid roll and counter-roll (i.e. the μ_1 and μ_2 axes are not too far off the roll axis). Thus, errors that derive from the fact that the kinematics from a rotating fly were replayed on a stationary robot would be particularly large for this degree of freedom. Other sources of error include the possible inaccuracies of our dynamics model, which did not include cross-terms and used damping coefficients based on steady-state approximations.

By mining the entire database, we were able to determine the pattern of wing motion that correlated with peak torque production around the μ_1, μ_2 and yaw axes (Fig. 6), and then to determine the relative contribution of the three wing angles to the moments by playing systematically distorted wing patterns through the robotic fly (Fig. 7). The results indicate that changes in the time history of the wing rotation angle, which strongly influences the angle of attack, are by far the most important for regulating torque about the μ_1, μ_2 and yaw axes (Fig. 7C,D). However, the torque modulations about the yaw axis and about the two axes in the stroke plane (μ_1 and μ_2) appear to occur via two distinct aerodynamic mechanisms (Fig. 8). As suggested by Bergou and co-workers (2010), changes in the mean offset of the wing rotation angle magnitude lower the angle of attack during one half-stroke while raising it on the other, thus producing an upstroke-to-downstroke imbalance in drag and thus net torque around the axis normal to the stroke plane. Although our results support this mechanism (Fig. 6A,D and Fig. 7A,B), we also found that the flies adjust the relative phase of wing rotation as well, thus creating additional yaw torque via unsteady mechanisms at stroke reversal (Dickinson et al., 1999; Sane and Dickinson, 2002). Flies also create torque about the μ_1 and μ_2 axes via changes in wing rotation angle, but in these cases the effect appears to be mediated almost entirely by changes in phase, and thus through unsteady effects at stroke reversal (Fig. 6E and Fig. 7C–F). One possible explanation for this difference is that changes in angle of attack during the translational portion of the stroke would be undesirable for regulating roll because they would generate large cross-talk in yaw torque.

A quite surprising result of our analysis was the relatively small importance of stroke amplitude and stroke deviation in the control of torque during saccades (Fig. 7C,D). This was particularly true for yaw torque, an observation that complicates interpretation of many tethered flight studies, which collectively show that flies generate large changes in stroke amplitude in response to both visual and mechanosensory rotations about the yaw axis (e.g. Sherman and Dickinson, 2003), as well as transient spontaneous changes that have been ubiquitously interpreted as fictive saccades. These changes in stroke amplitude were quite large and clearly correlated with yaw torque (Tammero, 2004). Why do tethered flies generate such large changes in stroke amplitude that do not seem necessary to generate yaw torque in free flight? One possibility is that the stroke amplitude signal measured during fictive saccades is indicative of the roll and pitch required for a banking maneuver, and not for yaw production per se. If true, this has immediate implications for the underlying circuitry as it is noteworthy that the stroke amplitude changes associated with fictive saccades are unidirectional, i.e. there is no evidence of an attempt at a programmed counter-rotation.

Recently, Schnell and co-workers (2014) suggested that the basic optomotor circuit in *Drosophila* includes an integral feedback term that might be mediated by Ca^{2+} dynamics in the terminals of the interneurons that encode horizontal rotation. Because the putative

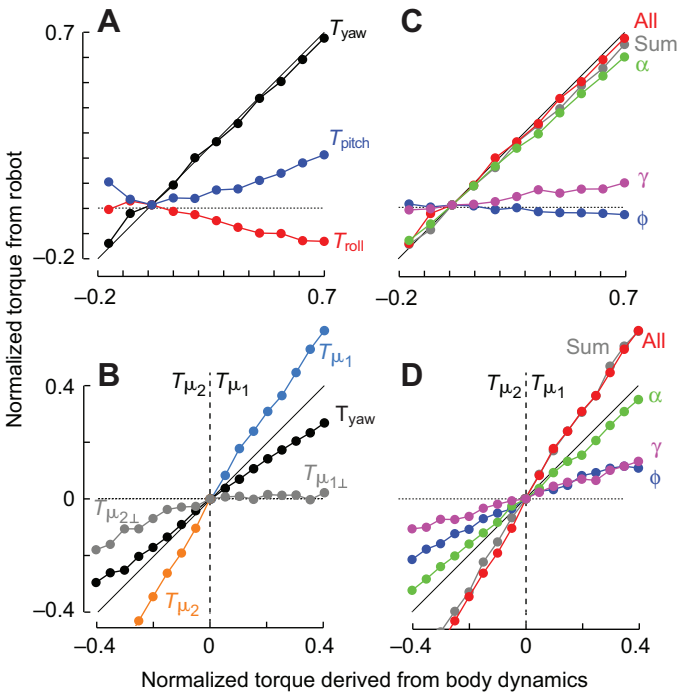

Fig. 7. Torques derived from body dynamics plotted against stroke-averaged torques measured using a robotic fly. The data are based on a graded series of wing kinematics that range from steady wingbeats to those that produce peak torque about the μ_1, μ_2 and yaw axes as shown in Fig. 6A–C. (A) Comparison of torque about the three principal body axes – yaw (T_{yaw}, black), roll (T_{roll}, red) and pitch (T_{pitch}, blue) – for the kinematics correlated with yaw production. (B) Comparison of torque about the μ_1 (blue), μ_2 (orange), $\mu_{1\perp}$ (gray), $\mu_{2\perp}$ (also gray) and yaw (black) axes. Positive values are for the kinematics correlated with control of torque about the μ_1 axis; negative values are for the kinematics that controls torque about the μ_2 axis. (C) Torques produced by varying the different wing kinematics parameters correlated with yaw torque control in isolation while maintaining all others at steady flight conditions. The effect of the different parameters is shown in blue (stroke angle ϕ), magenta (deviation angle γ) and green (rotation angle α). The gray trace is the sum of the torques for the separate cases; the red trace shows the case where all kinematics angles were varied together. The thin black solid line in all panels shows a match between torques determined from body dynamics and from wing kinematics played through the robot. (D) The same analysis as in C, but using the kinematics correlated with the control of torque about the μ_1 axis (positive values) and the μ_2 axis (negative values).

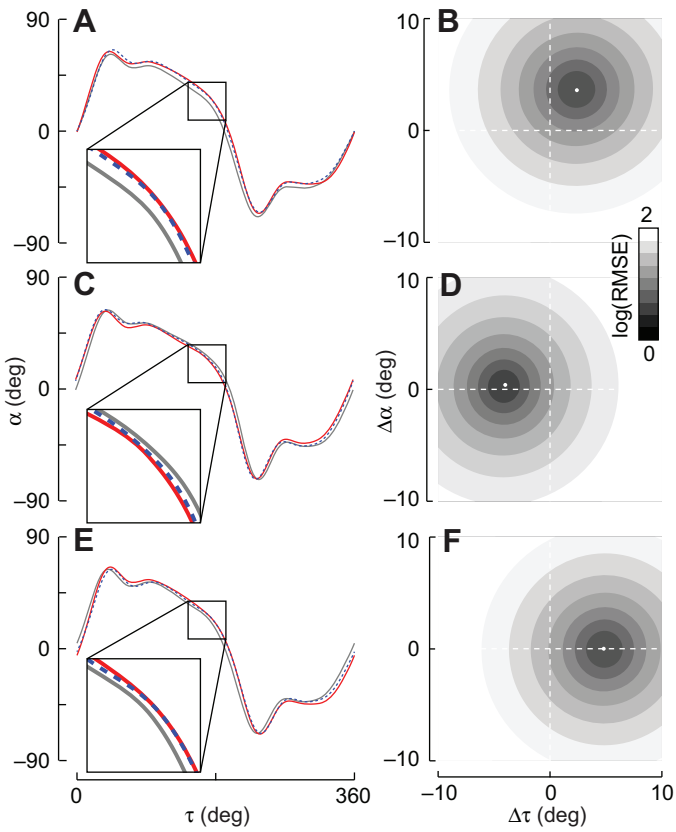

Fig. 8. Flies modulate the phase of wing rotation to control torque about the μ_1 and μ_2 axes, and modulate both the phase and offset of wing rotation to control torque about the yaw axis. (A) Wing rotation angle α of the right wing (red), left wing (gray) and left wing trace (blue) that has been translated along both the abscissa (wingbeat phase) and ordinate (rotation angle) to produce the lowest root mean squared error (RMSE) between the right and shifted left wing traces. (B) A plot of RMSE as a function of the plot of wingbeat phase Δτ (–10 deg<Δτ<10 deg) and mean wing rotation angle Δα (–10 deg<Δα<10 deg) for the kinematics correlated with peak yaw torque. Maximum correlation (minimum RMSE) is depicted by a white dot. RMSE is coded in gray on a logarithmic scale. (C,D) The same analysis as in A and B, but for the data correlated with peak torque about the μ_1 axis. (E,F) The same analysis as in A and B, but for the data correlated with peak torque about the μ_2 axis.

integrator winds up with prolonged stimulation, flies generate extremely large motor responses during typical open-loop optomotor experiments. Although this hypothesis explains why the optomotor responses in tethered flight are so large relative to the kinematics changes exhibited during free-flight maneuvers, it does not explain why flies generate such enormous changes in stroke amplitude when presented with stimuli that should elicit the production of yaw torque. Perhaps flies respond to visual rotation about the yaw axis by producing not just yaw torque but also roll torque, because they are attempting to turn via banking, as has been suggested by previous authors (Mronz and Lehmann, 2008). This hypothesis could be tested in the future by measuring free-flight responses to horizontal motion.

MATERIALS AND METHODS

Animals and experimental setup

The methods used in this study were identical to those described in detail elsewhere (Muijres et al., 2014) and are only briefly outlined here. Experiments were performed on 1–5 day old male and female *D. hydei*, from a laboratory stock reared on a 14 h:10 h light:dark cycle. Each day, approximately 50, 1 day old flies were released in the experimental chamber 4 h before their subjective dawn, after which experiments ran for 8 h. The experimental chamber consisted of a transparent cylindrical enclosure, surrounded by a panoramic array of green LED panels (Reiser and Dickinson, 2008) that provided a uniform illumination of 70 lx. Flies were filmed using three synchronized high-speed cameras (Photron SA5 with AF Nikor 60 mm lenses, lens aperture=*f*/22), which viewed the central portion of the arena from above and from two orthogonal side positions (Fig. 1A). The cameras operated at 7500 frames s^{-1} with an image resolution of 1024×1000 pixels, exposure time of 1/30,000 s, and image depth of 12 bits. Because of limitations in optics, the region of interest was restricted to a cube ~40 mm on each side. Each camera view was backlit using high-intensity infrared light panels, which were strobed in synchrony with every exposure. To maintain the inside temperature at ~25°C, we passed refrigerated air around the outside of the flight chamber. At the start and end of each 5 day recording period, we calibrated the camera system using direct linear transformation (DLT) (Christoph Reinschmidt; http://isbweb.org/software/movanal.html).

Throughout each experimental session, the cameras sampled continuously. When a fly flew directly through the center of the region of interest, it tripped an infrared laser cross-beam, which automatically triggered the storage of 372 ms of data both before and after the trigger

event. We captured more than 300 flight sequences, of which the majority consisted of a straight flight path, but occasionally a fly would perform a saccadic maneuver (supplementary material Movie 1). Although fruit flies are largely insensitive to infrared light, we were concerned that the high intensity of the infrared trigger lasers might elicit behavioral responses. For this reason, we only analyzed the saccades that flies initiated before passing through the trigger point. Given our sampling methods, we have no way of knowing whether any given saccade was elicited by visual expansion or via some internal stochastic event.

Measuring body and wingbeat kinematics

We manually selected 44 sequences from the entire data set for detailed analysis, which we subjectively classified as body saccades based on visual inspection of the raw video sequences. To extract kinematics throughout these saccades, we used an automatic machine-vision system as described in a recent analysis of escape maneuvers (Fig. 1B) (Muijres et al., 2014). The tracking routine provided us with Kalman-filtered estimates of the body and wing kinematics throughout each flight sequence (Fig. 1C; supplementary material Movie S2) (Muijres et al., 2014).

For all Kalman filters, the cross-product values in the error covariance matrices (**R** and **Q**) were set to zero, and measurement noise covariance matrix **R** was set to identity. Thus, adjusting the parameters in the process noise covariance matrix **Q** controlled Kalman smoothing. For positional data, we used a linear Kalman filter and the smoothing parameters of matrix **Q** were scaled according to a Taylor series. **Q** values corresponding to position were set to dt^2, velocity values were set to 1, and acceleration values were set to $1/dt^2$, where dt is the time step between two measurements (inverse of the frame rate).

To filter body and wing orientation data, we used an extended Kalman filter with two filtering steps (Yun and Bachmann, 2006), because quaternion update is non-linear. For body orientation filtering, we used the following **Q** parameters. For the first iteration, **Q** parameters associated with angular velocities and angular accelerations were set to zero, and parameters associated with quaternions were set to 0.003. For the second iteration, angular velocity parameters were set to 0.0001, angular acceleration parameters were set to $0.0001/dt^2$, and quaternion parameters were set to 1. For wing orientation filtering, we used a similar strategy but less smoothing was desired. For the first iteration, angular velocity parameters and angular acceleration parameters were set to zero, and quaternion parameters in **Q** were set to 1. For the second iteration, angular velocity parameters in **Q** were set to $1/dt^2$, angular acceleration parameters were set to 0 and quaternion parameters were set to 1.

Body position data thus consist of Kalman-filtered estimates of position, $\mathbf{X}(t)$, velocity, $\mathbf{U}(t)$, and linear acceleration, $\mathbf{a}(t)$. Based on $\boldsymbol{U}(t)$ and $\mathbf{a}(t)$, we determined the start and end of each saccade by estimating horizontal accelerations normal and tangential to the flight path [$a_N(t)$ and $a_T(t)$, respectively]. Using an expectation maximization-based clustering analysis on $a_N(t)$ and $a_T(t)$ for all measured flight sequences (Muijres et al., 2014), we divided flight sequences into steady and maneuvering segments, such that steady segments satisfied $a_N<0.19\,g$ and $-0.17\,g<a_T<0.14\,g$, where g is gravitational acceleration. The times at which a saccade starts (t_{start}) and ends (t_{end}) were defined as the moments when body acceleration passed these threshold values. Note that these points in time do not encompass the entire length of the maneuver, but the method enabled us to systematically and objectively define and align the saccades.

Based on the velocity data, we determined flight heading, $\sigma(t)$, which we used to determine the turn angle, $\Delta\sigma$, for each saccade. $\mathbf{U}(t)$ was also used to determine changes in flight speed, $dU(t)$, throughout the maneuver relative to the start of each sequence. Linear acceleration, $\mathbf{a}(t)$, was used to estimate the direction, σ_a, and magnitude, a_{hor}/g, of normalized acceleration within the horizontal plane, as well as the magnitude of the vertical acceleration, a_z/g. Body orientation was expressed in the body Euler angles (yaw, ψ_E; pitch, θ_E; and roll, η_E) in the world reference frame and normalized angular velocity of the body, $\mathbf{\Omega}=\{\omega_x, \omega_y, \omega_z\}$, in the body reference frame (Fig. 1C). All rotation rates were normalized using f_{steady}, where f_{steady} is the wingbeat frequency during steady flight for *D. hydei* (~189 Hz; from Muijres et al., 2014).

Each tracked wingbeat was expressed by the wingbeat frequency, f, and three Euler angles within the body reference frame: wing stroke angle ϕ, stroke deviation angle γ and wing rotation angle α (Fig. 1C). Note that all body and wing orientation variables are defined relative to the stroke plane, which is defined as horizontal during steady flight (Fig. 1C). For *D. hydei*, this is at an inclination angle of 47.5 deg relative to the long axis of the body (Muijres et al., 2014).

Estimating aerodynamic forces and torques based on body dynamics

The aerodynamic forces throughout a flight maneuver can be estimated directly from body accelerations as:

$$\mathbf{F}(t) = (\mathbf{a}(t) + \mathbf{g})/|\mathbf{g}|, \tag{1}$$

where **F** is the aerodynamic force vector normalized with body weight, mg, and $\boldsymbol{g}=\{0,0,g\}$ is the gravitational acceleration vector. The orientation of this force vector in the body frame was defined as the roll (ξ) and pitch (β) angle of **F** relative to the stroke plane normal (Fig. 1C), and was calculated based on the body Euler angles and **F**.

The aerodynamic torque produced throughout a maneuver was estimated from the body rotations. Because aerodynamic damping has been shown to be an important source of passive stability in flapping flight (Hesselberg and Lehmann, 2007; Hedrick et al., 2009), we estimate normalized torque $\boldsymbol{T}$ using a linear model based on both normalized angular velocities and accelerations:

$$\mathbf{T}(t) = \mathbf{C}\mathbf{\Omega}(t) + \mathbf{I}\,\dot{\mathbf{\Omega}}(t), \tag{2}$$

where $\dot{\mathbf{\Omega}}$ is the angular acceleration vector of the body normalized by f^2_{steady}, and which is estimated by numerically differentiating $\mathbf{\Omega}$. **C** is the aerodynamic damping coefficient matrix normalized by mgl/f_{steady}, where l is wing length, and **I** is the body inertia matrix normalized by mgl/f^2_{steady}. Because aerodynamic torque produced by a wing scales with the product of force and wing length, we normalized torque by $|\mathbf{a}+\mathbf{g}|ml$. We modeled **C** as:

$$\mathbf{C} = \begin{bmatrix} C_{roll} & 0 & 0 \\ 0 & C_{pitch} & 0 \\ 0 & 0 & C_{yaw} \end{bmatrix}, \tag{3}$$

and **I** as:

$$\mathbf{I} = \begin{bmatrix} I_{roll} & 0 & 0 \\ 0 & I_{pitch} & 0 \\ 0 & 0 & I_{yaw} \end{bmatrix}. \tag{4}$$

Thus, our simplified model assumes that all interaction coefficients in both **C** and **I** are negligible.

The damping coefficients in **C** were based on damping estimates for *D. melanogaster* reported in the literature (Cheng et al., 2009; Dickson et al., 2010). The yaw-damping coefficient for *D. hydei* (C_{yaw}) was estimated by scaling values measured for *D. melanogaster* using a robotic model (Dickson et al., 2010). Roll and pitch damping for *D. hydei* were based on computational estimates of damping coefficients in *D. melanogaster* (Cheng et al., 2009). For consistency among the damping coefficients for the three degrees of freedom, we first linearly scaled all damping coefficients estimated for *D. melanogaster* by Cheng et al. (2009) equally, such that yaw damping was equal to that reported by Dickson et al. (2010), and then scaled these values to the slightly larger species, *D. hydei*. This resulted in the following normalized roll, pitch and yaw damping coefficients: C_{roll}=0.22, C_{pitch}=0.08, C_{yaw}=0.41. Note that the damping coefficient for yaw is 5 times greater than that for pitch and twice as large as that for roll.

Inertia coefficients within the stroke plane reference frame were estimated based on a cylindrical body model with body mass m and pitch angle of 47.5 deg and a wing model consisting of a horizontal disk divided into 100 concentric rings (Fig. 1C). Each ring has a homogeneously distributed mass equal to the mass of the local spanwise wing section plus its added fluid mass. Following Ellington (1984), total wing mass was estimated as 5% of body mass, and added mass was equal to a cylindrical fluid mass circumventing

each wing section. This resulted in normalized roll inertia I_{roll}=0.64, normalized pitch inertia I_{pitch}=1.07 and normalized yaw inertia I_{yaw}=0.57.

Correlating wingbeat kinematics with torque production

To determine how a fly controls torque throughout a saccade, we correlated changes in wing kinematics with torques estimated from body dynamics (Eqn 2). Wing kinematics were correlated with torque about an axis defined by a torque vector, $\mathbf{T}'$, by parsing the complete dataset into steady wingbeats and wingbeats in which the fly generated some absolute magnitude of $\mathbf{T}'$ ($|\mathbf{T}'|$) that was larger than one standard deviation of the entire distribution of $|\mathbf{T}'|$ for all wingbeats in the dataset. Changes in kinematics angles throughout a wingbeat relative to the steady wingbeat angles were linearly correlated with the stroke-averaged normalized torque estimated from body dynamics (Eqn 2) as:

$$\mathrm{mod}(\kappa, \mathbf{T}')_i = (\kappa_i - \kappa_{\mathrm{steady}})/|\mathbf{T}'|_i, \quad (5)$$

where $\mathrm{mod}(\kappa,\mathbf{T}')_i$ is the wingbeat modification variable for kinematics angle κ (representing ϕ, γ or α) of the ith wingbeat in the dataset of $|\mathbf{T}'|$ producing wingbeats. κ_{steady} is the equivalent kinematics angle distribution of the average steady wingbeat of *D. hydei*, based on 1603 wingbeats measured by Muijres et al. (2014) (Fig. 1D).

Variation in wingbeat frequency (which is equal for the two wings) is excluded from this analysis because such modulation could not alter torque directly. By fitting a Fourier series through the complete dataset of $\mathrm{mod}(\kappa,\mathbf{T}')$, we determined the average wing kinematics modulation distributions, $\mathrm{MOD}(\kappa,\mathbf{T}')$ for each kinematics angle and torque axis. Fourier series were fitted using a Levenberg–Marquardt algorithm and are defined as:

$$\kappa(t^*) = a_0 + \sum_{n=1}^{N} a_n \cos(2\pi n t^*) + b_n \sin(2\pi n t^*), \quad (6)$$

where a_n and b_n are the Fourier series coefficients for the nth order, and t^* is normalized time for each wingbeat ($t^*=tf$). All Fourier series [$\mathrm{MOD}(\phi,\mathbf{T}')$, $\mathrm{MOD}(\gamma,\mathbf{T}')$, $\mathrm{MOD}(\alpha,\mathbf{T}')$] were 8th order ($N$=8). From the $\mathrm{MOD}(\kappa,\mathbf{T}')$ estimates, the set of wing kinematics variables that would result in a given amount of torque $|\mathbf{T}'|$ about torque axis $\mathbf{T}'$ can be reconstructed by:

$$\kappa = \kappa_{\mathrm{steady}} + |\mathbf{T}'|\mathrm{MOD}(\kappa, \mathbf{T}'). \quad (7)$$

Measuring aerodynamic forces and torques using a dynamically scaled robot

Apart from estimating aerodynamic forces and torques from body dynamics (Eqns 1 and 2, respectively), we also estimated forces and torques from wing kinematics, using a dynamically scaled robot in a fixed body reference frame (Dickinson et al., 1999). This technique enabled us to study the aerodynamics of saccadic maneuvers in a systematic and detailed manner. We replayed the wingbeat kinematics in a fixed body reference frame because aerodynamic and inertial effects of body rotations were modeled using Eqn 2. Note that aerodynamics effects due to body translations were ignored.

To assess the accuracy of our methods, we compared torque measurements based on the wingbeat kinematics with the torque estimates based on body dynamics (Eqn 2). This analysis was performed on two sets of data. The first dataset consisted of the mean wing kinematics and body dynamics throughout the average saccade, estimated by aligning the wingbeats from all maneuvers. This enabled us to test qualitatively whether the measured changes in wingbeat kinematics captured the forces and torques produced throughout the saccade. The second dataset was based on the systematic analysis described above, in which we correlated wingbeat kinematics with torque production. Using Eqn 7, we constructed a set of kinematics patterns that should produce a systematically increasing amount of body torque about a specific body axis $\mathbf{T}'$. The range of body torques was chosen such that it captured the complete behavioral envelope of measured torque production. We defined a body torque distribution spanning a range from zero body torque (steady flight) to a torque equal to approximately three times the standard deviation of the $|\mathbf{T}'|$ distribution for all measured wingbeats, and parsed it into eight values. For each, we created the matching deformed wingbeat kinematics using Eqn 7. We then replayed the set of systematically distorted wing kinematics on the robotic fly and measured the resulting stroke-averaged forces and torques about all three orthogonal body axes, and compared these values with the values of body torques. This approach also enabled us to determine cross-talk between torque modulations about the different orthogonal axes. The distributions of $|\mathbf{T}'|$ and the corresponding wing kinematics constructed using Eqn 7 were also used to study the effects of stroke, deviation and wing rotation angle on torque production. Using a method similar to that described by Muijres et al. (2014), we systematically modulated one wing kinematics variable, while maintaining steady kinematics for the other angles, and replayed these on the robot.

Cases in which body torque was equal to three standard deviations of the $|\mathbf{T}'|$ distribution, which we considered as an estimate for peak torque production, were analyzed in more detail using two complementary methods. First, we replayed the wingbeat kinematics that corresponded to this peak torque (estimated using Eqn 7) on the robot and measured force and torque throughout the wingbeat. Second, we analyzed the changes in wing kinematics that result in peak torque production. For each kinematics angle, the difference in kinematics between the left and right wing might result from temporal phase shift, from a shift in the mean value, or from higher order modulations in the time history (Fig. 1D). For each kinematics variable, we estimated the temporal phase shift and offset in mean value between the left and right wing by systematically translating the left wing data along the time (τ) and ordinate (κ) axes. For each combination of $\Delta\tau$ and $\Delta\kappa$, we determined the root mean square error (RMSE) between the right wing and shifted left wing values. The combination of $\Delta\tau$ and $\Delta\kappa$ at which RMSE was minimum defines the phase shift and angular offset between left and right wing for that wing kinematics angle and $|\mathbf{T}'|$ axis combination. The corresponding magnitude of RMSE quantifies how well the wing kinematics modulations are described by $\Delta\tau$ and $\Delta\kappa$, relative to any higher order modulations.

Acknowledgements
The authors wish to thank Johan Melis, Steve Safarik and Darren Howell for help with this project.

Competing interests
The authors declare no competing or financial interests.

Author contributions
F.T.M. and M.H.D. planned experiments and wrote the paper. F.T.M. and N.A.I. collected data in flight arena, ran the automated machine vision tracking software and identified sequences with saccadic turns. M.J.E. collected data using the robotic fly. F.T.M. analyzed the data, with the help of M.J.E. and M.H.D.

Funding
This research was supported by grants (to M.H.D.) from the Air Force Office of Scientific Research (FA9550-10-1-0368), the Paul G. Allen Family Foundation, and the US Army Research Laboratory (DAAD 19-03-D-0004) and (to F.T.M.) the Swedish Research Council (Vetenskapsrådet).

Supplementary material
Supplementary material available online at
http://jeb.biologists.org/lookup/suppl/doi:10.1242/jeb.114280/-/DC1

References
Bender, J. A. and Dickinson, M. H. (2006). A comparison of visual and haltere-mediated feedback in the control of body saccades in *Drosophila melanogaster*. *J. Exp. Biol.* **209**, 4597-4606.
Bergou, A. J., Ristroph, L., Guckenheimer, J., Cohen, I. and Wang, Z. J. (2010). Fruit flies modulate passive wing pitching to generate in-flight turns. *Phys. Rev. Lett.* **104**, 148101.
Censi, A., Straw, A. D., Sayaman, R. W., Murray, R. M. and Dickinson, M. H. (2013). Discriminating external and internal causes for heading changes in freely flying *Drosophila*. *PLoS Comput. Biol.* **9**, e1002891.
Cheng, B., Fry, S. N., Huang, Q., Dickson, W. B., Dickinson, M. H. and Deng, X. (2009). Turning dynamics and passive damping in flapping flight. *2009 IEEE Int. Conf. Robot. Autom.* 1889-1896.
Cheng, B., Fry, S. N., Huang, Q. and Deng, X. (2010). Aerodynamic damping during rapid flight maneuvers in the fruit fly *Drosophila*. *J. Exp. Biol.* **213**, 602-612.
Collett, T. S. and Land, M. F. (1975). Visual control of flight behaviour in the hoverfly, *Syritta pipiens*. *J. Comp. Physiol. A* **99**, 1-66.
David, C. T. (1978). The relationship between body angle and flight speed in free-flying *Drosophila*. *Physiol. Entomol.* **3**, 191-195.

Dickinson, M. H. (1999). Haltere-mediated equilibrium reflexes of the fruit fly, *Drosophila melanogaster*. *Philos. Trans. R. Soc. Lond. B Biol. Sci.* **354**, 903-916.
Dickinson, M. H. (2014). Death valley, *Drosophila*, and the Devonian toolkit. *Annu. Rev. Entomol.* **59**, 51-72.
Dickinson, M. H., Lehmann, F.-O. and Sane, S. P. (1999). Wing rotation and the aerodynamic basis of insect flight. *Science* **284**, 1954-1960.
Dickson, W. B., Polidoro, P., Tanner, M. M. and Dickinson, M. H. (2010). A linear systems analysis of the yaw dynamics of a dynamically scaled insect model. *J. Exp. Biol.* **213**, 3047-3061.
Ellington, C. P. (1984). The aerodynamics of hovering insect flight. I. The quasi-steady analysis. *Philos. Trans. R. Soc. Lond. B Biol. Sci.* **305**, 1-15.
Elzinga, M. J., van Breugel, F. and Dickinson, M. H. (2014). Strategies for the stabilization of longitudinal forward flapping flight revealed using a dynamically-scaled robotic fly. *Bioinspir. Biomim.* **9**, 025001.
Fry, S. N., Sayaman, R. and Dickinson, M. H. (2003). The aerodynamics of free-flight maneuvers in *Drosophila*. *Science* **300**, 495-498.
Götz, K. G. and Wandel, U. (1984). Optomotor control of the force of flight in *Drosophila* and *Musca*. *Biol. Cybern.* **51**, 135-139.
Hateren, J. and Schilstra, C. (1999). Blowfly flight and optic flow. II. Head movements during flight. *J. Exp. Biol.* **1500**, 1491-1500.
Hedrick, T. L., Cheng, B. and Deng, X. (2009). Wingbeat time and the scaling of passive rotational damping in flapping flight. *Science* **324**, 252-255.
Hesselberg, T. and Lehmann, F.-O. (2007). Turning behaviour depends on frictional damping in the fruit fly *Drosophila*. *J. Exp. Biol.* **210**, 4319-4334.
Land, M. F. (1999). Motion and vision: why animals move their eyes. *J. Comp. Physiol. A. Sens. Neural Behav. Physiol.* **185**, 341-352.
Maye, A., Hsieh, C.-h., Sugihara, G. and Brembs, B. (2007). Order in spontaneous behavior. *PLoS ONE* **2**, e443.
Mronz, M. and Lehmann, F.-O. (2008). The free-flight response of *Drosophila* to motion of the visual environment. *J. Exp. Biol.* **211**, 2026-2045.
Muijres, F. T., Elzinga, M. J., Melis, J. M. and Dickinson, M. H. (2014). Flies evade looming targets by executing rapid visually directed banked turns. *Science* **344**, 172-177.
Nalbach, G. (1994). The halteres of the blowfly *Calliphora* II. Three-dimensional organization of compensatory reactions to real and simulated rotations. *J. Comp. Physiol. A* **175**, 695-708.
Reiser, M. B. and Dickinson, M. H. (2008). A modular display system for insect behavioral neuroscience. *J. Neurosci. Methods* **167**, 127-139.
Reiser, M. B. and Dickinson, M. H. (2013). Visual motion speed determines a behavioral switch from forward flight to expansion avoidance in *Drosophila*. *J. Exp. Biol.* **216**, 719-732.
Reynolds, A. M. and Frye, M. A. (2007). Free-flight odor tracking in *Drosophila* is consistent with an optimal intermittent scale-free search. *PLoS ONE* **2**, e354.
Ristroph, L., Bergou, A. J., Ristroph, G., Coumes, K., Berman, G. J., Guckenheimer, J., Wang, Z. J. and Cohen, I. (2010). Discovering the flight autostabilizer of fruit flies by inducing aerial stumbles. *Proc. Natl. Acad. Sci. USA* **107**, 4820-4824.
Sane, S. P. and Dickinson, M. H. (2002). The aerodynamic effects of wing rotation and a revised quasi-steady model of flapping flight. *J. Exp. Biol.* **205**, 1087-1096.
Schilstra, C. and Hateren, J. (1999). Blowfly flight and optic flow. I. Thorax kinematics and flight dynamics. *J. Exp. Biol.* **1490**, 1481-1490.
Schnell, B., Weir, P. T., Roth, E., Fairhall, A. L. and Dickinson, M. H. (2014). Cellular mechanisms for integral feedback in visually guided behavior. *Proc. Natl. Acad. Sci. USA* **111**, 5700-5705.
Sherman, A. and Dickinson, M. H. (2003). A comparison of visual and haltere-mediated equilibrium reflexes in the fruit fly *Drosophila* melanogaster. *J. Exp. Biol.* **206**, 295-302.
Stewart, F. J., Baker, D. A. and Webb, B. (2010). A model of visual-olfactory integration for odour localisation in free-flying fruit flies. *J. Exp. Biol.* **213**, 1886-1900.
Tammero, L. F. (2004). Spatial organization of visuomotor reflexes in *Drosophila*. *J. Exp. Biol.* **207**, 113-122.
Tammero, L. F. and Dickinson, M. H. (2002). The influence of visual landscape on the free flight behavior of the fruit fly Drosophila melanogaster. *J. Exp. Biol.* **205**, 327-343.
van Breugel, F. and Dickinson, M. H. (2012). The visual control of landing and obstacle avoidance in the fruit fly *Drosophila melanogaster*. *J. Exp. Biol.* **215**, 1783-1798.
van Breugel, F. and Dickinson, M. H. (2014). Plume-tracking behavior of flying *Drosophila* emerges from a set of distinct sensory-motor reflexes. *Curr. Biol.* **24**, 274-286.
Wagner, H. (1986). Flight performance and visual control of flight of the free-flying housefly (*Musca domestica* L.) III. Interactions between angular movement induced by wide- and smallfield stimuli. *Philos. Trans. R. Soc. Lond. B Biol. Sci.* **312**, 581-595.
Wehrhahn, C., Poggio, T. and Bülthoff, H. (1982). Tracking and chasing in houseflies (*Musca*). *Biol. Cybern.* **45**, 123-130.
Yun, X. and Bachmann, E. R. (2006). Design, implementation, and experimental results of a quaternion-based Kalman filter for human body motion tracking. *IEEE Trans. Robot.* **22**, 1216-1227.

Fig. S1. Temporal dynamics of body rotations throughout the saccadic maneuver. Rotational dynamics of the fly body are described as angular positions (A-C), normalized angular velocities (D-F) and normalized angular accelerations (G-I) about the principal body axes (roll axis, pitch axis and yaw axis as defined in Fig. 1C). The temporal dynamics of the angular positions were estimated by integrating angular velocities in the body reference frame (integration constant was set to zero at the start of each track); angular velocities were normalized by the wingbeat frequency at steady flight, f_{steady}, estimated by Muijres et al. (2014); angular accelerations were estimated by differentiating angular velocities, and were normalized by the steady wingbeat frequency f^2_{steady}. Grey lines show data from all measured saccades, and black lines with grey bars are means and 95% confidence intervals for all trails.

Fig. S2. Torque dynamics within the stroke plane throughout the saccadic maneuver. Torque dynamics is described by the temporal dynamics of torque about the primary torque axis μ_1 (A) and its orthogonal axis $\mu_{1\perp}$ (B), and by the temporal dynamics of torque about the counter-torque axis μ_2 (C) and its orthogonal axis $\mu_{2\perp}$ (D). All torques are normalized by $|\boldsymbol{a}+\boldsymbol{g}|ml$; grey lines show data from the separate saccades, and black lines with grey bars are means and 95% confidence intervals for all trails. The vertical dotted line defines the point in time where torque in the stroke plane is approximately zero, and that therefore separates the primary rotation phase and the counter-rotation phase (t=12.5 ms).

Fig. S3. Correlation between the wingbeat kinematics angles of the left and right wing, for the kinematics that results in peak yaw torque (left column), peak torque about the primary μ_1 axis (middle column), and peak torque about the counter-torque axis μ_2 (right column). (A-C) kinematics angles of the right wing (red), the original kinematics of the left wing (grey), and the translated left wing kinematics for which correlation between the wingbeat kinematics angles of the left and right wing were maximal (blue dotted traces). (D-L) root mean squared error (RMSE) based on the difference between the left and right wing kinematics angle throughout the measured phase shift range $-10° < \Delta\tau < 10°$ and mean kinematics angle shift range $-10° < \Delta\kappa < 10°$ (maximum correlation at minimum RMSE is depicted by a white dot): (D-F) for stroke angle; (G-I) for deviation angle; (J-L) for wing rotation angle. Logarithmic values of RMSE are scaled according to the scale bar in (L).

Movie 1. Top view of a fruit fly performing a saccadic maneuver. The movie is slowed down 100 times, and every third recorded frame is shown. The turn angle of this saccade is approximately 90 degrees, which is close to the average saccadic turn angle for all trails.

Movie 2. Body and wings model of a fruit fly performing a saccadic maneuver. The movie is slowed down 300 times. The turn angle of this saccade is approximately 90 degrees, which is close to the average saccadic turn angle for all trails.

Movie 3. A movie of all 44 flight tracks overlaid on top of each other, viewed from below. The movie is slowed down 100 times, and traces are color-coded with time according to the scale bar in Fig. 1E. Note that all left-handed turns have been mirrored into right-handed turns, and all sequences were aligned according to position and heading at the start of the saccadic maneuver (t_{start} = 0 ms).

Movie 4. A movie of all 44 flight tracks overlaid on top of each other, viewed from the side. The movie is slowed down 100 times, and traces are color-coded with time according to the scale bar in Fig. 1E. Note that all left-handed turns have been mirrored into right-handed turns, and all sequences were aligned according to position and heading at the start of the saccadic maneuver (t_{start} = 0 ms).

Movie 5. A movie of all 44 flight tracks overlaid on top of each other, viewed from behind. The movie is slowed down 100 times, and traces are color-coded with time according to the scale bar in Fig. 1E. Note that all left-handed turns have been mirrored into right-handed turns, and all sequences were aligned according to position and heading at the start of the saccadic maneuver (t_{start} = 0 ms).

Movie 6. A movie of all 44 flight tracks overlaid on top of each other, in perspective view. The movie is slowed down 100 times, and traces are color-coded with time according to the scale bar in Fig. 1E. Note that all left-handed turns have been mirrored into right-handed turns, and all sequences were aligned according to position and heading at the start of the saccadic maneuver (t_{start} = 0 ms).

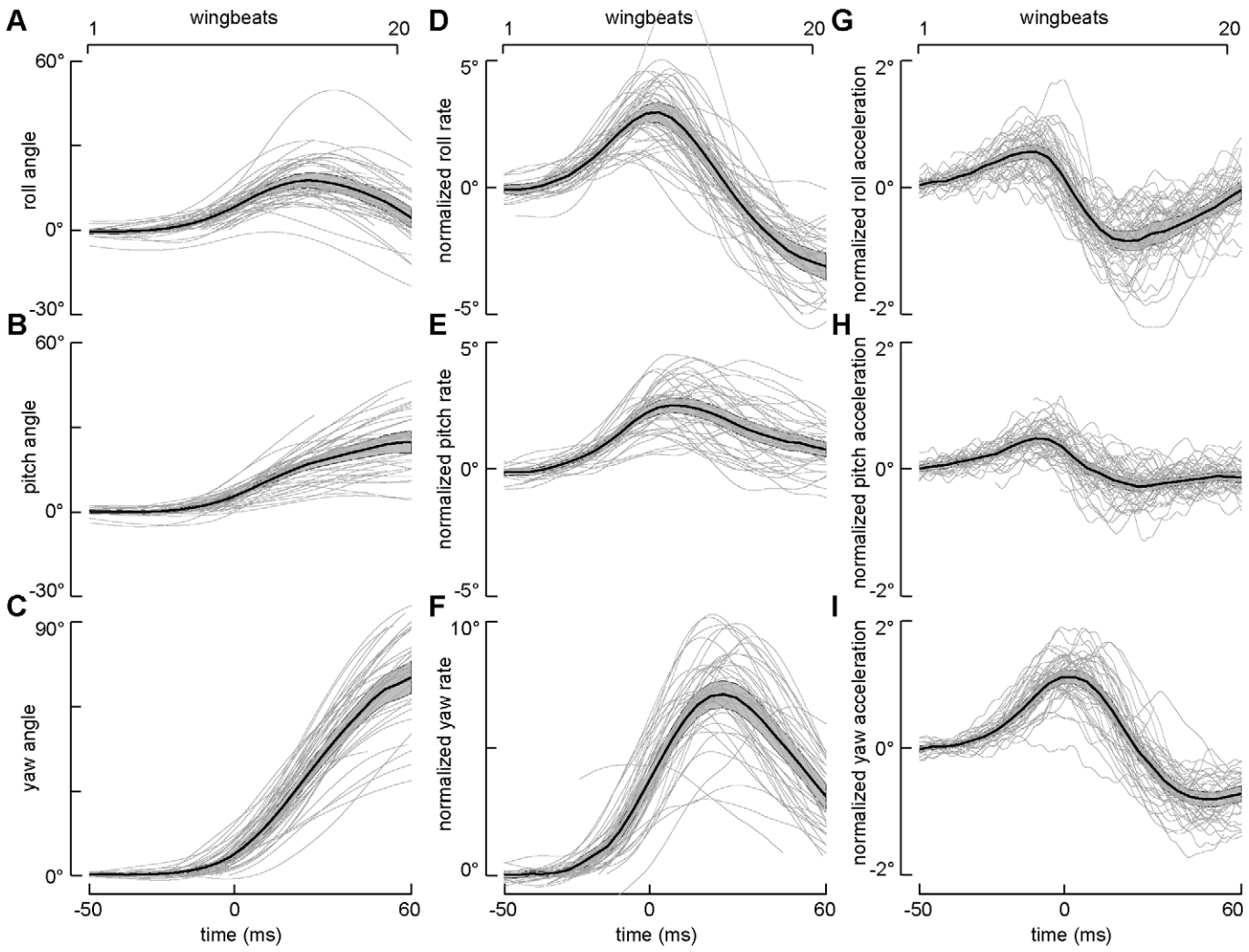

Figure S1

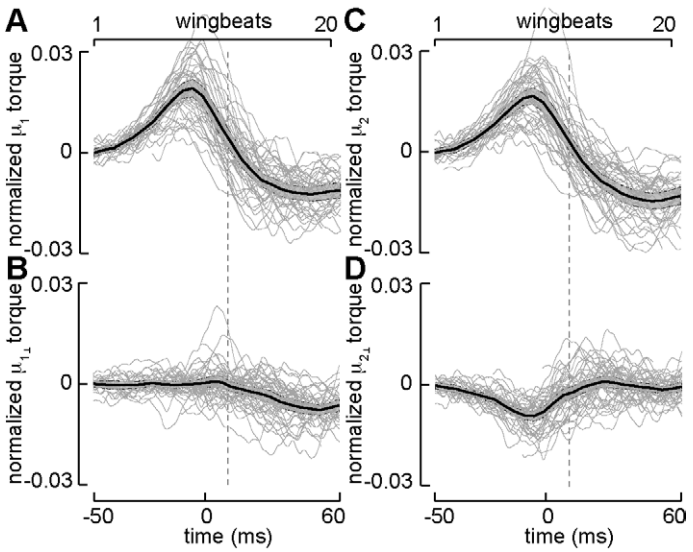

Figure S2

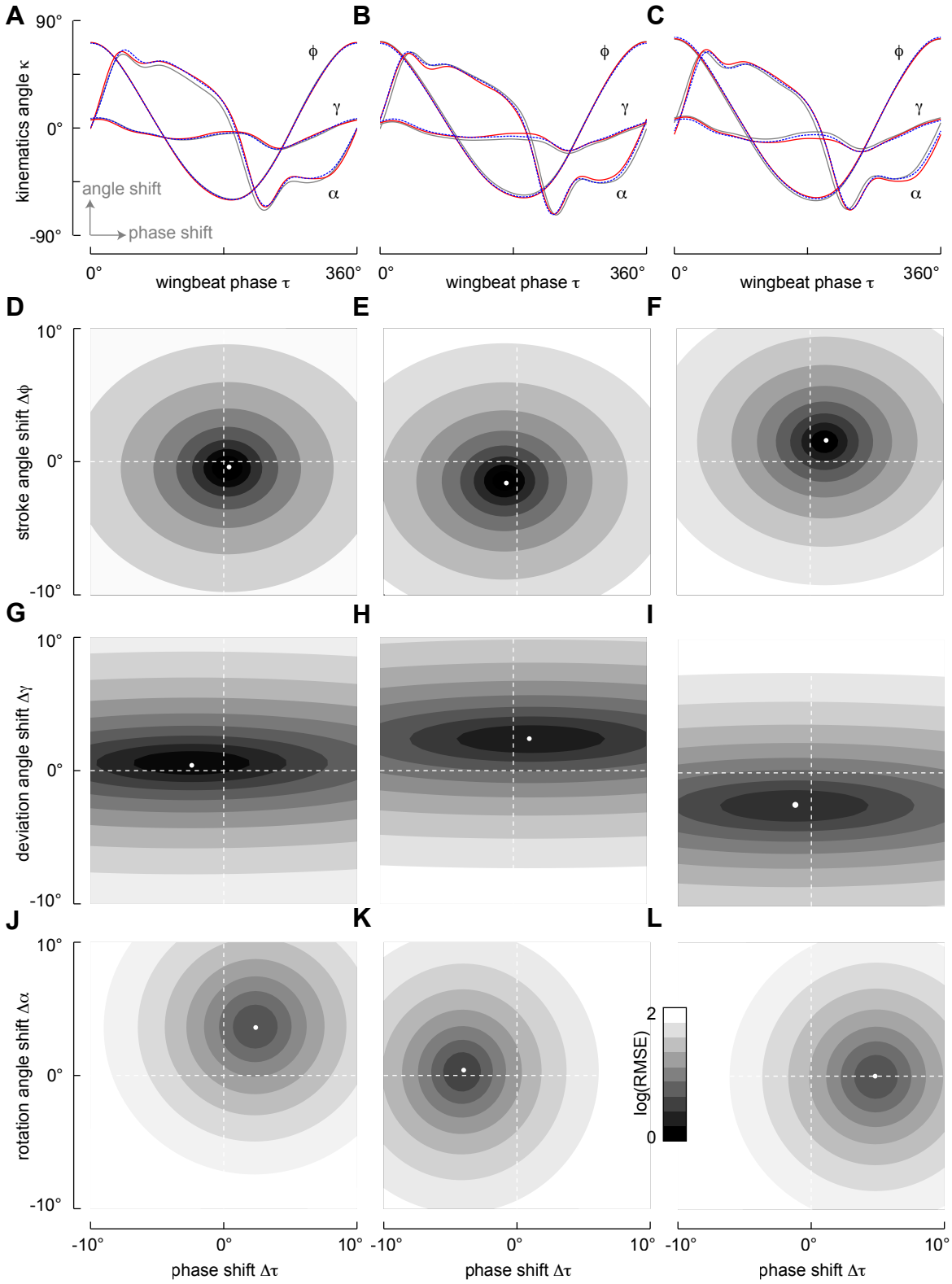
A
B
C
90°
0°
-90°
kinematics angle κ
ϕ
γ
α
angle shift
phase shift
0°
wingbeat phase τ
360°
D
E
F
10°
0°
-10°
stroke angle shift Δϕ
G
H
I
deviation angle shift Δγ
J
K
L
rotation angle shift Δα
log(RMSE)
2
0
phase shift Δτ

Figure S3

Movie 1.

Movie 2.

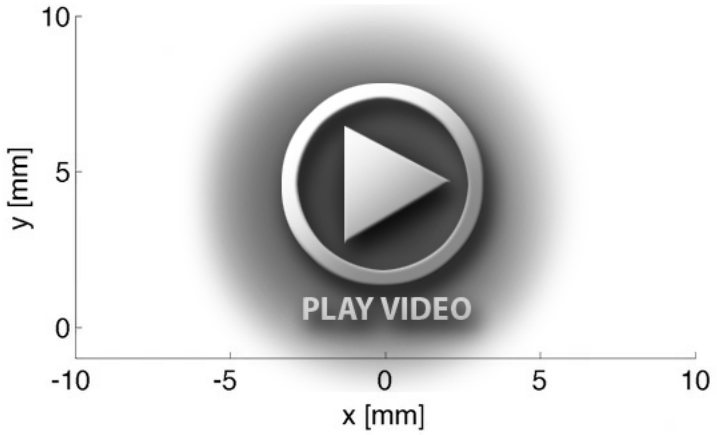

Movie 3.

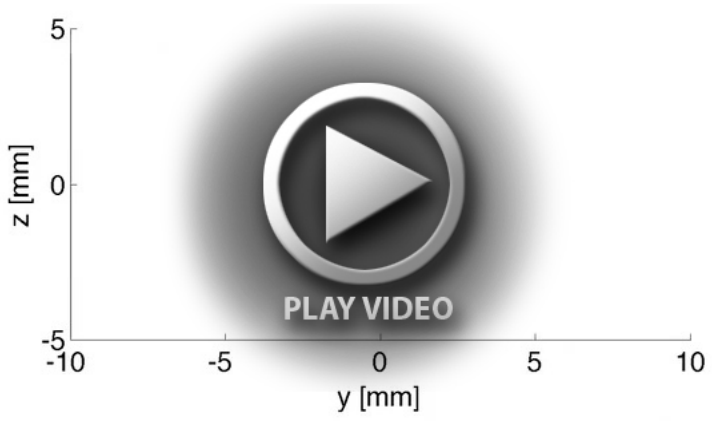

Movie 4.

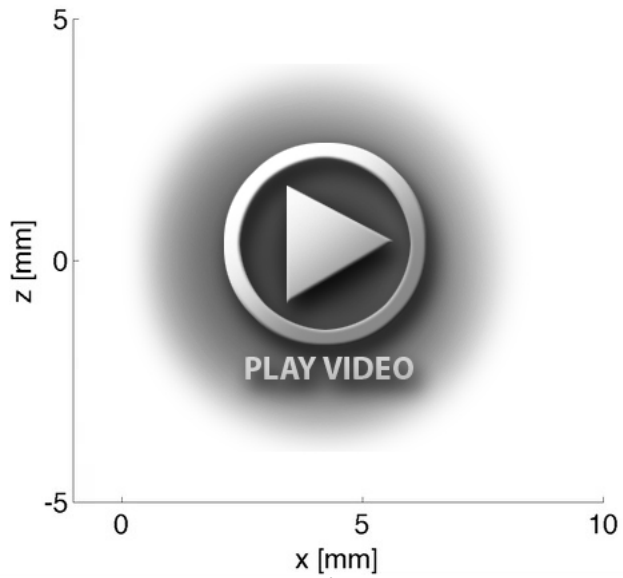

Movie 5.

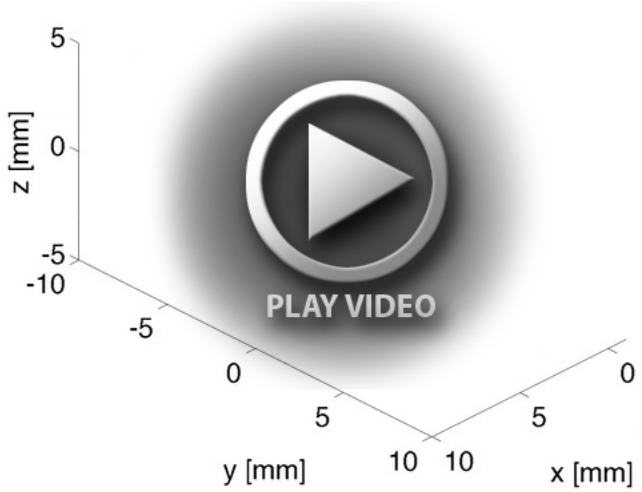

Movie 6.